GOLD Observations of Longitudinal Variations in the Nighttime Equatorial Ionization Anomaly (EIA) Crests Latitudes

R. W. Eastes[1], D. K. Karan[1], C. E. Martinis[2], R. E. Daniell[3], Q. Gan[1], A. G. Burns[4], and W. E. McClintock[1]

[1]Laboratory for Atmospheric and Space Physics, University of Colorado, Boulder, CO, USA,
[2]Center for Space Physics, Boston University, Boston, MA, USA,
[3]Ionospheric Physics, Stoughton, MA, USA,
[4]High Altitude Observatory, National Center for Atmospheric Research, Boulder, CO, USA,

Corresponding author: Richard Eastes (richard.eastes@lasp.colorado.edu)

Key Points:

- Observed nighttime EIA crests latitudes over South America decrease with increasing magnetic longitude near 26° (47° W geographic)
- The average decrease, ~2°, suggests that the influence of equatorial electric fields over South America decreases as longitude increases
- Crest latitudes sometimes show periodic changes of approximately six days that may indicate the influence of mesospheric waves

Abstract

Each day the GOLD (Global-scale Observations of the Limb and Disk) imager observes the Equatorial Ionization Anomaly (EIA) near sunset from ~8° E to ~80° W geographic longitude. Most images cover ~45° of longitude (~3 hours), and most longitudes are observed multiple times. The variation of EIA crests latitude with longitude during March 2020 has been analyzed. A significant, ~2° change in the average separation of the EIA crests occurs near 26° magnetic longitude (47° W geographic), where the geographic and geomagnetic equators cross. The crests are more separated westward of the equators crossing. This indicates that the influence of the equatorial electric field varies substantially with longitude in this region. In addition, near 26° longitude the latitude of the northern EIA crest is ~1° higher, but the difference systematically decreases with longitudinal distance from there. Also, day-to-day trends in the separation are seen during some periods of the month.

Plain Language Summary

Each day the GOLD (Global-scale Observations of the Limb and Disk) imager observes the nighttime Equatorial Ionization Anomaly (EIA) near sunset as the terminator progresses from Africa to across South America. Most images cover ~45° of longitude (~3 hours of local time), and most longitudes are observed multiple times. The longitude dependence of the EIA crests latitude during March 2020 has been analyzed. A significant, ~2° change in the average separation of the EIA crests occurs near 26° magnetic longitude (47° W geographic), where the geographic and geomagnetic equators cross. The crests are more widely separated to the West. This indicates that the influence of the equatorial electric field varies with longitude in this region. In addition, near 26° magnetic longitude the latitude of the northern EIA crest is ~1° higher, but systematically decreases with longitudinal distance from there. Also, day-to-day trends in the separation suggest that the latitudes may be influenced by 6-day waves in the mesosphere.

1 Introduction

Longitudinal variations in the EIA radiance have been linked to similar variations in the equatorial electrojet (EEJ) strength that are attributable to longitudinal differences in solar tidal forcing (England et al., 2006; Fang et al., 2009; Jin et al., 2008; Lühr et al., 2008; Pedatella, Hagan, et al., 2012; Lühr & Manoj, 2013). Variations in the optical dayglow emission radiances at EIA north-crest latitude over Indian longitudes show a similar relationship with the EEJ strength (Karan et al., 2016). The small scale (3^o-7^o) longitudinal differences in the dayglow radiances are attributed to variations of the equatorial electric fields (Karan et al., 2017). However, the longitudinal variability of the EIA crest latitude, i.e. the peak radiance of the crests, is less studied, and the longitudinal changes in EEJ strength that have been credited with changing the EIA radiance may also change its latitude. Each night GOLD provides images of the EIA crests. These observations provide an opportunity to better understand the longitudinal and temporal variations in the latitude of the EIA crests and possibly the equatorial electric (E) fields.

While periodic variations in the EIA crests as a function of longitude are sometimes seen (e.g., Eastes et al., 2019, Fig 3; Gan et al 2020, Fig. 2), equally striking are occasional decreases in their separation (e.g., Basu et al., 2009) which are also seen in the GOLD observations. In random examinations of the data such occurrences were most frequently seen east of ~47° West geographic longitude (glon) where the geographic and geomagnetic equators cross. Such decreases have sometimes been sufficient to reduce the two crests typically observed to a single crest located

near the magnetic equator. Since the equatorial E field strength is associated with the latitude of the EIA, an interesting question is: what can the EIA latitude as a function of longitude tell us about the influence of E fields at low latitudes?

Earth's electric fields in the ionosphere-thermosphere are not sufficiently understood, and the equatorial fields have been examined in several recent papers (e.g., Soares, et al., 2018; Wang, et al., 2020) using models and observations in efforts to understand the effects of geometry and tides. Recently, Rodríguez-Zuluaga, et al. (2020) found that the EIA crest latitudes observed by GOLD sometimes exhibit a mesoscale structure (a few thousand km scale size), indicating that the EIA crest latitudes are influenced by atmospheric waves from the lower atmosphere.

During the first two years of observations by the GOLD mission, geomagnetic conditions have been exceptionally quiet. Each evening the mission observes the same region of the EIA near sunset with sufficient signal-to-noise to determine the EIA latitude over South America, the Atlantic Ocean, and West Africa. This paper presents our analysis of observations from March 2020, a month with no significant geomagnetic activity with the goal of better understanding what additional insights GOLD observations of the EIA crests latitude may provide.

2 Data

The observations used in the analysis are partial disk scans of the nightside by the GOLD imager, which is hosted on the SES 14 satellite in geostationary orbit at 47.5° W. The instrument and its observations have been described by McClintock et al. (2020a, b) and Eastes et al. (2017, 2020). Each of the two, independent channels contains a scan mirror and interchangeable slits, enabling them to observe either the north or south hemisphere.

GOLD conducts nightside imaging observations (partial disk scans, NI1 mode) daily, beginning at 1700 satellite local time (LT, 2010 UT) with a 30-min cadence, using only one channel (designated as channel B), alternating between the northern and southern hemispheres. At 2000 LT (2310 UT), when both channels are used for nightside scans, the cadence increases to 15-min for simultaneous imaging of both hemispheres. This imaging continues until 2130 LT (0040 UT) when observations are suspended to avoid opportunities to accidentally observe the Sun. Each night 24 images (each covering half the latitudes) are obtained. The medium-resolution slit used during the partial-disk scans provides ~0.3 nm spectral resolution and a spatial resolution of ~93 km (96 km × 80 km) at the sub-satellite location. Observations were made at a constant angular resolution.

Most individual scans cover ~45° in longitude, ~3 hours in local time, just east of the sunset terminator. Scans shift westward throughout the evening, observing the low latitudes from ~8° E to ~80° W longitude. At EIA latitudes the western edge of each scan images the EIA ~1 hour after sunset. The observation sequence is explained in detail by Karan et al., 2020. At night the EIA typically appears as bands of enhanced OI 135.6 nm emission, one on each side of the magnetic equator. An example of the EIA images (from March 30, 2020) can be seen in Figure 1a. The emission altitude for OI 135.6 nm is assumed to be 300 km, a typical altitude for the F region peak, when geolocating the pixels. An example of the EIA crest latitudes obtained from the nightly sequence of images is shown in Figure 1b where each data point represents a peak in the crest brightness (the method is described in Section 3).

The OI 135.6 nm emission from the EIA is produced by recombination of atomic oxygen ions and electrons in the Earth's ionosphere. In the F region oxygen ions are the dominant ion

species. Since the emission rate varies as $n_e \times n_{O^+}$, approximately as the square of the electron density, the observed radiance is dominated by emissions from near the peak in electron density and is indicative of the peak plasma density N_{max} and its spatial variation.

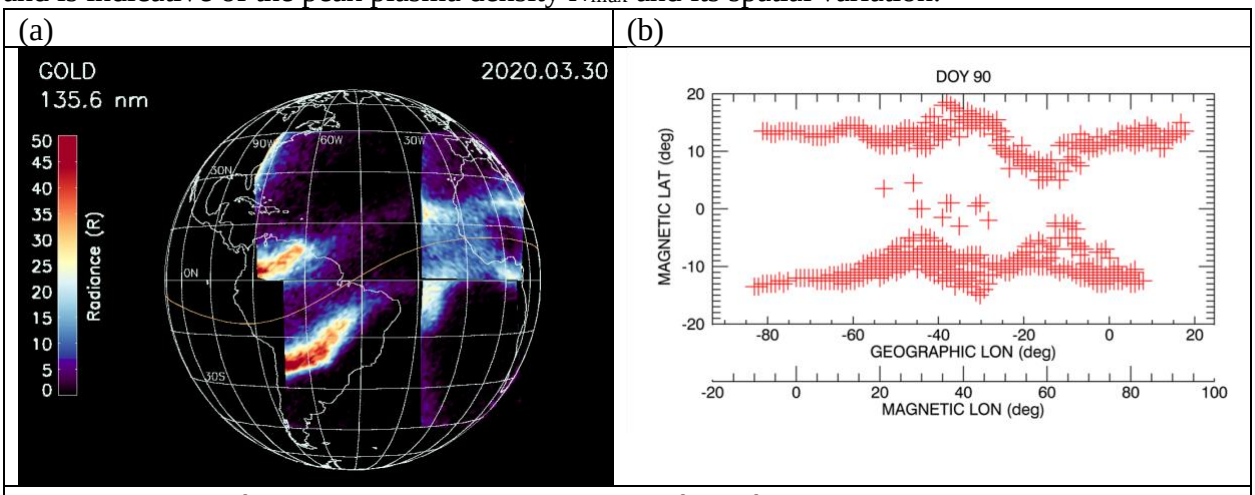

Figure 1. (1a, left) Composite image constructed from four nightside (NI1) images taken on March 30, 2020. The geographic latitude variation of the EIA crests with geographic longitude seen in these images included in the crest, peak latitudes shown in (1b) as determined after mapping into magnetic coordinates. (1b, right) All crest, peak latitudes identified in nightside images from March 30, 2020 (DOY 90) at latitudes within 20° of the magnetic equator are included in the analysis. At most longitudes there are multiple images of the crests.

This paper examines the nightside observations during March 2020. This month was chosen because it is near equinox, a period when bright emissions are observed from the EIA. Bright emissions best allow an accurate and consistent determination of the EIA crest latitudes. Also, the geomagnetic conditions, which can be a significant influence on the EIA crest latitude, during the month were relatively quiet. The Dst and ap indices are shown in Figure 2. Some geomagnetic activity is observed on days 79 and 91, but has little effect on the distribution of the EIA crests. Although abrupt and significant changes in the location of the EIA crests have been observed previously (see Figure 4 from Eastes et al., 2019), such drastic changes were not detected in these observations. In addition, the F10.7 index, also shown in Figure 2, indicates that the solar irradiance was low and varied little.

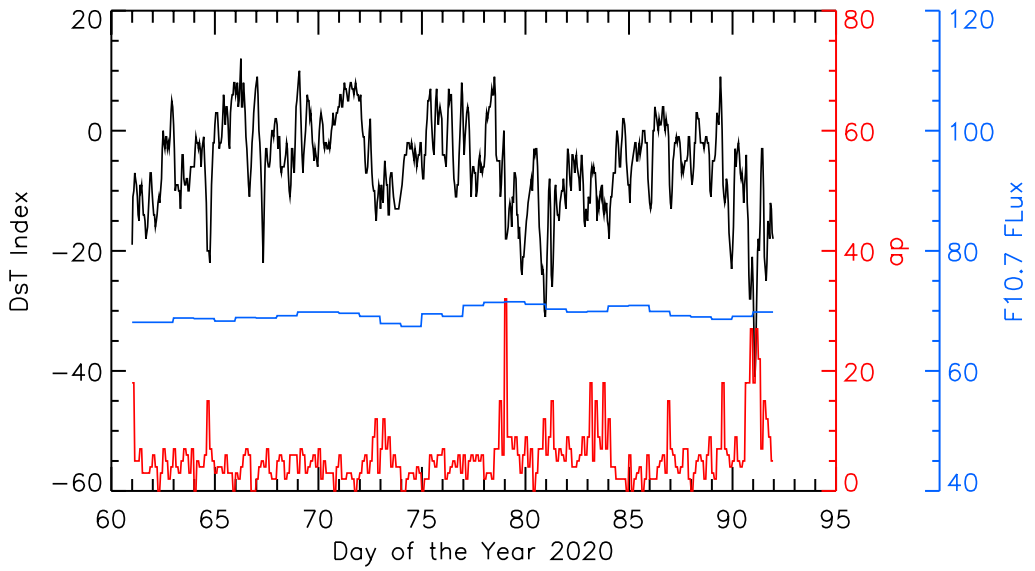

Figure 2. Geophysical data for March 2020 (DOY 61-91), the time period of the observations analyzed. The Dst and ap indexes are plotted in black and red, respectively. The F10.7 index is plotted in blue.

3 Analysis Method

While the GOLD data are mapped into geographic coordinates during processing, the EIA is analyzed in magnetic coordinates since it is oriented along Earth's magnetic equator. Thus, we calculated the quasi-dipole (QD) geomagnetic coordinates (Laundal and Richmond, 2017) corresponding to the geographic coordinates from the IGRF 2018 scalar potentials (Thébault et al., 2015). Applying this transformation, all images are remapped into geomagnetic coordinates. A one day sequence of such images is shown in supplementary Figure S1. From the remapped images, the OI 135.6 nm radiance as a function of magnetic latitude (mlat) is obtained for each 1^{o} in magnetic longitude (mlon). These radiances are smoothed over 3 points (i.e., 1.5^{o} in mlat), and the maxima correspond to the EIA crests latitudes used in subsequent analysis. Following this procedure, EIA crests latitudes from all 24 images are obtained each night. One example, from March 30, is shown in Figure 1b.

Longitudes near the western edge of South America are measured only once each night (see the data points near 80 W in Figure 1b). Other longitudes are sampled multiple times, 4-5 at most longitudes, during the night. Consequently, multiple crest latitudes are identified on a given night (see Figure S1). While there is some variation in the EIA crests latitudes, due to the signal-to-noise limitations of the data, the latitudinal changes with longitude shown in Figure 1b are consistent with the images shown in Figure 1a and the other images (Figure S1) from March 30. A similar correspondence is typically seen throughout March 2020. This indicates that much of the latitude variation with longitude depends on the EIA development at local times at or prior to the earliest observations. The earliest local times observed at equatorial latitudes by GOLD in the March 2020 NI1 images was ~1 hour after sunset. Therefore, during GOLD's observations (1700-2130 LT at the satellite; March 30, 2010 UTC to March 31, 0040 UTC) the observed crest latitudes are more indicative of the crest latitudes at earlier local times than of latitude changes during 1700-2130 LT. While the EIA brightness typically decreases with time due to recombination, the

variation of EIA latitude with longitude appears to persist from the earliest to the latest observations.

Before further processing, the crest latitudes in each 1° mlon bin for a day (e.g., as in Figure 1b) were filtered to remove extraneous crest latitudes. Filtering removed latitudes deviating by more than half the mean value (when ≥ 3 latitudes were available in the hemisphere) and any latitudes > 20° mlat from the magnetic equator. From the remaining EIA crest latitudes, a daily mean was calculated for each hemisphere, north and south, using 5° longitude bins. The 31-day, monthly average of the crests mlat (magnitude) as a function of mlon is shown in Figure 3. Magnetic latitudes of the northern crest and absolute value of the southern crest are plotted as red +'s and blue x's, respectively. The average mlat of the crests (north and south) is plotted as green ○'s. As would be expected, daily variability is substantial in the observations, but deviations from the 3 day means are only ~0.2°.

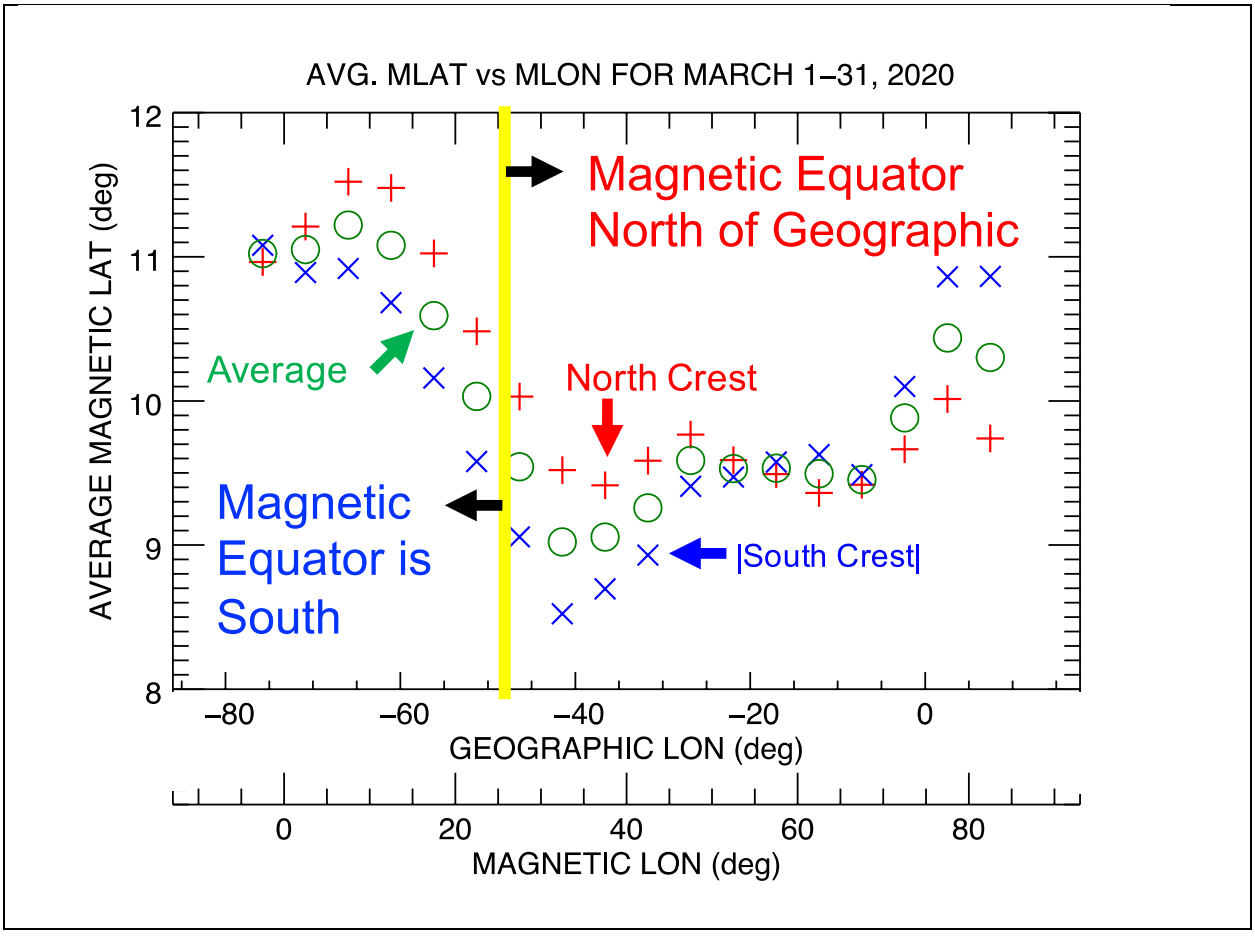

Figure 3. Monthly average of the absolute value of the magnetic latitude of the EIA crest as a function of magnetic longitude (green ○). Also shown are the magnetic latitudes of the northern crest (red +), and absolute value of southern crest (blue ×). (See text for a complete explanation of the averaging process). The yellow vertical line at 26.5° mlon indicates the longitude where the magnetic and geographic equators cross. Higher latitudes west of the yellow line indicate that the effects of equatorial electric fields are stronger than the ones to the East.

4 Results and Discussion

As shown in Figure 3, between 5° and 35° mlon (-70° to -40° W glon) there are significant changes in both the average latitude of the EIA crests and the asymmetry of the crest locations. The average latitude of the crests decreases as magnetic longitude increases until a minimum near 35° mlon, after which the latitude increases slowly with longitude. Each of the crests, north and south, exhibits a slightly different longitude dependence. A north-south asymmetry in the crests latitudes steadily increases with longitude from 5° mlon, until 35° mlon. Both hemispheres show an almost identical change with longitude, and between 5° mlon and 35° mlon the northern crests are ~1° further from the equator than the southern crests. Then the asymmetry steadily decreases until ~50° mlon. Between ~ 50° and 70° mlon the crests are symmetric. Further east the asymmetry is reversed and the southern crests are furthest from the equator.

The EIA characteristics, like crests location and symmetry with respect to the magnetic equator, depend on the combined effects of ionosphere production and loss rates (primarily at local times prior to sunset), neutral winds, magnetic field configuration and electric fields. Since the EIA latitudes are averages for a month of observations during a solar minimum period without notable changes in solar irradiance, changes in production are not expected to be a significant influence. Longitude variations of neutral winds effects are a more likely to cause changes. Asymmetries due to meridional winds have been reported (e.g., Khadka et al., 2018 and references therein), and zonal winds can also cause asymmetries due to magnetic declination differences. Winds from HWM 14 (Drob et al., 2015) 1 hour after sunset during March, are similar at locations near the maximum (~75° W) and minimum (~25° W) separations of the crests with northward winds reaching ~40 m/s and zonal winds of ~100 m/s at latitudes near the EIA. While winds might shift the crest latitudes northward, resulting in higher northern crest latitudes (red + in Figure 3), the longitudinal differences shown in Figure 3 seem inconsistent with longitudinally uniform winds. The northward displacement of the crests occurs only between ~75° W and ~25° W glon. Between ~25° W and ~5° W no displacement is observed, i.e. the crests are symmetric, and at the easternmost longitudes the opposite displacement is observed: the southern EIA crest is furthest from the equator.

Even if the winds were longitudinally uniform, the magnetic field is not. The region GOLD is sampling presents the largest changes in the configuration of the Earth's magnetic field. At the westernmost and easternmost longitudes the magnetic declination δ is near zero. Near the region where magnetic and geographic equators cross, δ is ~20-25°. These longitude changes in magnetic declination could be related to some of the patterns observed in Figure 3. An important aspect when dealing with meridional winds is to understand how they interact with the direction of the magnetic field lines. Along magnetic meridians, the effects of the winds can vary longitudinally even in the absence of longitudinal variations in the winds. If we denote the geographic zonal and

meridional wind components as U_G and V_G, then the geomagnetic meridional compoent can be expressed as $V_M = V_G \cos(\delta) \mp U_G \sin(\delta)$ (equation 3 of Luan and Solomon, 2008). Note that, the meridional wind components positive when they are equatorward, that is southward directed in the northern hemisphere and northward in the southern hemisphere, and the upper (lower) sign applies to the northern (southern) hemisphere. Thus V_M can be very different than V_G if δ is nonzero and a strong zonal wind is present. Thus large asymmetries in the crests can occur, and their longitude variation will depend on the local magnetic field configuration. The increase in the asymmetry in the American sector may be related to the increase in magnetic declination until the longitude of the equators crossing. Eastward from it, now V_M decreases and the asymmetry also decreases, until it reaches zero and the crests are symmetric. Eastward of longitudes with symmetric crests, the separation increases, but the direction is opposite to that in the American sector. At these eastward longitudes magnetic declination is near zero again and the geographic equator is north of the magnetic equator. If the meridional winds are southward, then the asymmetry observed can be explained. HWM14 showed that the meridional winds were 40 m/s. However, no groundbased data for the African and Atlantic sectors have been incorporated in HWM14, and observations suggest those sectors may differ from HWM14. A study by Fisher et al., (2015) reported Fabry-Perot Interferometer measurements from the Ukaimeden Observatory in Morocco (31.2° N, 7.87°W; geomagnetic: 19.7°) from Nov 2013 to Dec 2014. Average meridional winds for March were southward at ~40 m/s. While F10.7 was higher (~120) during those observations, similar winds during March 2020 near 10° E could explain the asymmetry observed by GOLD.

Winds can influence the vertical drifts, which have been linked to the strength of the EIA, but few studies have investigated the longitude dependence of the drifts. Fejer et al. (2008) have shown that equinox evening upward drifts increase from ~ 70° W to 0° (see their Figure 8). Therefore, these observations do not explain the results from Figure 3. Kil et al. (2009) used ROCSAT-1 data to extract vertical plasma drifts near the equator and found a wave-4 pattern that was used to reproduce similar pattern in electron density distribution (Fang et al., 2009). Signatures of this extensively studied "wave-4" structure include a longitudinal peak in the electron density over South America. The latitude changes observed by GOLD are also in that region. The longitudinal trend in the crest latitudes from GOLD is similar to those seen in topside isodensity contours from ROCSAT-1, as reported by Kil et al. (2008) for March, 1999-2002 and Kp$\leq$3+ (their Figure 1e). They saw more widely separated contours at ~73° than at ~25° W glon. The tide producing the wave-4 structure would be a persistent influence on the vertical winds, which are not well quantified. Neutral density changes associated with the wave-4 structure, reported by Liu et al. (2009), suggest that the longitudinal structure of the crests might also be influenced by changes in the composition. They detected longitude dependent neutral density perturbations, with a peak near 45° W glon (e.g., their Figure 1b). If there are also corresponding composition changes, the electron densities would be affected. They also saw correlated electron density changes that would be consistent with such composition changes; however, composition changes have not been sufficiently bounded to accurately quantify their influence.

Additional insights may be obtained from the day-to-day changes in the average crests magnetic latitude as a function of longitude, shown in Figure 4. The daily EIA crests latitudes are plotted versus magnetic and geographic longitudes (in Figure 3 the monthly average of these daily EIA crests latitudes is shown as green circles). In these daily data a ~6-day periodicity is seen in peak latitudes. For instance, at 20° mlon, the averaged EIA crests are located at a higher latitude on days 67, 71, and 76, compared to the days in between. This westward propagating, 5-6-day

modulation of the F-region EIA may be related to the quasi-6-day waves (Q6DWs) arising from the stratosphere-mesosphere.

Observational and modeling studies have found that Q6DWs are exceptionally active around equinox (Liu et al. 2004; Gan et al., 2015; 2018). At these same longitudes Yamazaki et al. (2020) recently reported a 6-day period in 2019, Fall-equinox observations by SWARM. Coupling of the 6-day periodicity from the terrestrial atmosphere to the F-region ionosphere is beyond the scope of this paper. Gan et al. (2016) and Forbes et al. (2018) provide further details on such coupling. Recently, a similar coupling signature involving planetary waves with the post-sunset EIA crests on a day-to-day scale, was identified in the GOLD data (Gan et al., 2020), demonstrating that large-scale waves (planetary waves and tides) are detectable in the GOLD observations.

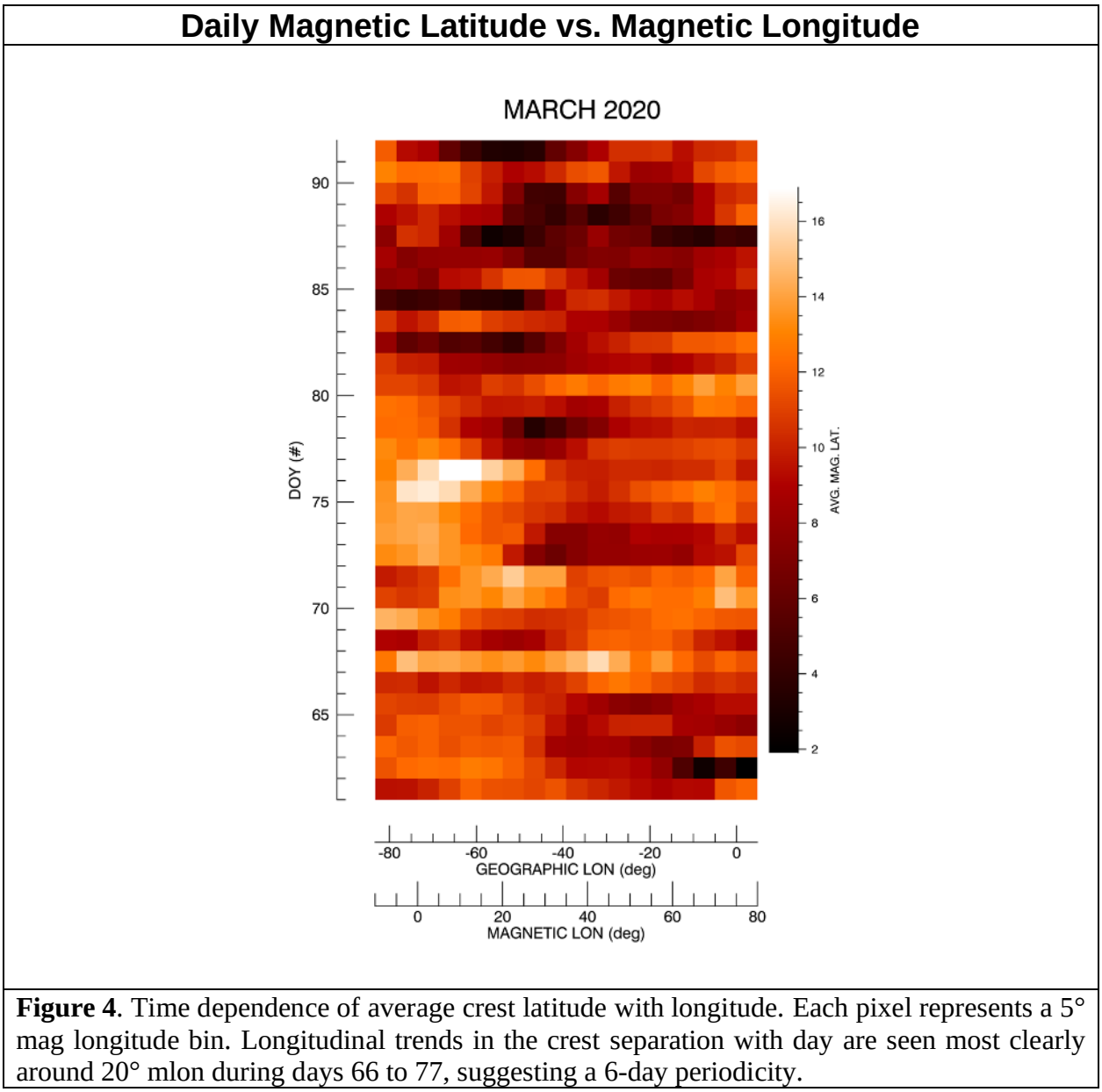

Figure 4. Time dependence of average crest latitude with longitude. Each pixel represents a 5° mag longitude bin. Longitudinal trends in the crest separation with day are seen most clearly around 20° mlon during days 66 to 77, suggesting a 6-day periodicity.

5 Conclusions

Examination of GOLD nightside disk observations (NI1) during March 2020, a geomagnetically quiet period shows a distinct variation in the monthly average EIA crest latitude with longitude and a 6-day period in the daily observations. In the monthly average (Figure 3), the average crests latitudes are ~2° higher west of 26° magnetic longitude (47° W geographic) than to the east. This change suggests that the influence of the potential drivers varies with longitude and may be related to the varying geomagnetic field configuration in the longitudes sampled. These changes appear to be consistent with prior observations that have been associated with a wave-4 structure in the low latitude ionosphere and thermosphere. Avenues for a wave-4 structure to influence the nighttime ionosphere, e.g. composition changes in the neutral atmosphere, must be examined further to establish the mechanisms responsible for the changes observed. In addition, distinct latitudinal differences are also seen in the individual northern and southern crests. Their magnetic latitudes differ by ~1° (north furthest from the equator) at longitudes near 26° while at other longitudes there is no difference or it is reversed, with the southern crests furthest from the equator.

The daily changes in crest latitude with longitude observed by GOLD, shown in Figure 4, suggest that the data may also provide additional insight into the influence of the lower atmosphere on Earth's ionosphere-thermosphere system. A 6-day period, most prominent early in the month, consistent with quasi-6-day waves that have previously been observed in the mesosphere. Other, similar mesospheric influences have been indicated by previous analyses of GOLD data. Together, these results provide new insights into the ionosphere-thermosphere system and the influences on the Earth's nighttime ionosphere.

Acknowledgments and Data

The geomagnetic indices and solar flux data are obtained from https://omniweb.gsfc.nasa.gov/. The GOLD data used in this study are available from the GOLD Science Data Center (http://gold.cs.ucf.edu/search/) and NASA's Space Physics Data Facility (https://spdf.gsfc.nasa.gov). This research was supported by NASA contract 80GSFC18C0061to the University of Colorado.

References

Alken, P., A. Maute, A. D. Richmond, H. Vanhamäki, & G. D. Egbert (2017). An application of principal component analysis to the interpretation of ionospheric current systems, *J. Geophys. Res. Space Physics*, *122*, 5687–5708, doi:10.1002/ 2017JA024051

Basu, Su., S. Basu, J. Huba, J. Krall, S. E. McDonald, J. J. Makela, E. S. Miller, S. Ray, and K. Groves (2009), Day-to-day variability of the equatorial ionization anomaly and scintillations at dusk observed by GUVI and modeling by SAMI3, J. Geophys. Res., 114, A04302, doi:10.1029/2008JA013899

Drob, D. P., Emmert, J. T., Meriwether, J. W., Makela, J. J., Doornbos, E., Conde, M., et al. (2015). An update to the Horizontal Wind Model (HWM): The quiet time thermosphere, *Earth and Space Science*, *2*, 301–319, doi:10.1002/2014EA000089

Eastes, R. W., McClintock, W. E., Burns, A. G., Anderson, D. N., Andersson, L., Codrescu, M., et al. (2017). The Global-scale Observations of the Limb and Disk (GOLD) mission. *Space Sci Rev*, 212, 383, doi:10.1007/s11214-017-0392-2

Eastes, R. W., Solomon, S. C., Daniell, R. E., Anderson, D. N., Burns, A. G., England, S. L., Martinis, C. R., & McClintock, W. E. (2019). Global-scale observations of the equatorial ionization anomaly. *Geophysical Research Letters, 46, 9318-9326.* https://doi.org/10.1029/2019GL084199*h*

Eastes, R. W., McClintock, W. E., Burns, A. G., Anderson, D. N., Andersson, L., Aryal, S., et al. (2020). Initial observations by the GOLD mission. *J. Geophys. Res. Space Physics*, *125*, e2020JA027823. https://doi.org/ 10.1029/2020JA027823

England, S. L., Maus, S., Immel, T. J., & Mende, S. B. (2006). Longitudinal variation of the *E* region electric fields caused by atmospheric tides. *Geophysical Research Letters*, *33*, L21105. https://doi.org/10.1029/2006GL027465

Fang, T.-W., Kil, H., Millward, G., Richmond, A. D., Liu, J.-Y., & Oh, S.-J. (2009). Causal link of the wave-4 structures in plasma density and vertical plasma drift in the low-latitude ionosphere. *J. Geophys. Res. Space Physics*, *114*, A10315. https://doi.org/10.1029/2009JA014460

Fejer, B. G., Jensen, J. W., and Su, S. (2008). Seasonal and longitudinal dependence of equatorial disturbance vertical plasma drifts, *Geophysical Research Letters*, *35*, L20106. https://doi.org/10.1029/2008GL035584, 2008

Fisher, D. J., J. J. Makela, J. W. Meriwether, R. A. Buriti, Z. Benkhaldoun, M. Kaab, and A. Lagheryeb (2015), Climatolo- gies of nighttime thermospheric winds and temperatures from Fabry-Perot interferometer mea- surements: From solar minimum to solar maximum, *J. Geophys. Res. Space Physics*, *120*, 6679–6693, doi:10.1002/2015JA021170.

Forbes, J. M., Zhang, X., Bruinsma, S., & Oberheide, J. (2013). Lunar semidiurnal tide in the thermosphere under solar minimum conditions. *J. Geophys. Res. Space Physics*, *118*, 1788–1801. https://doi.org/10.1029/2012JA017962

Forbes, J. M., Maute, A., Zhang, X., & Hagan, M. E. (2018). Oscillation of the ionosphere at planetary-wave periods. *J. Geophys. Res. Space Physics*, 123, 7634–7649. https://doi.org/10.1029/2018JA025720

Gan, Q., Yue, J., Chang, L. C., Wang, W. B., Zhang, S. D., & Du, J. (2015). Observations of thermosphere and ionosphere changes due to the dissipative 6.5-day wave in the lower thermosphere. *Annales Geophysicae, 33*(7), 913-922. doi:10.5194/angeo-33-913-2015

Gan, Q., W. Wang, J. Yue, H. Liu, L. C. Chang, S. Zhang, A. Burns, and J. Du (2016), Numerical simulation of the 6 day wave effects on the ionosphere: Dynamo modulation, *J. Geophys. Res. Space Physics*, 121, 10,103–10,116, doi:10.1002/2016JA022907

Gan, Q., Oberheide, J., & Pedatella, N. M. (2018). Sources, Sinks, and Propagation Characteristics of the Quasi 6-Day Wave and Its Impact on the Residual Mean Circulation. *J. Geophys. Res. Atmospheres, 123*(17), 9152-9170. doi:10.1029/2018jd028553

Gan, Q., Eastes, R. W., Burns, A. G., Wang, W., Qian, L., Solomon, S. C., et al. (2020). New observations of large‐scale waves coupling with the ionosphere made by the GOLD Mission: Quasi‐16‐day wave signatures in the F‐region OI 135.6‐nm nightglow during sudden stratospheric warmings. *J. Geophys. Res. Space Physics*, 125, e2020JA027880. https://doi.org/10.1029/2020JA027880

Jin, H., Miyoshi, Y., Fujiwara, H., & Shinagawa, H. (2008). Electrodynamics of the formation of ionospheric wave number 4 longitudinal structure. *J. Geophys. Res. Space Physics*, *113*, A09307. https://doi.org/10.1029/2008JA013301

Karan, D. K., D. Pallamraju, K. A. Phadke, T. Vijayalakshmi, T. K. Pant, and S. Mukherjee (2016). Electrodynamic influence on the diurnal behavior of neutral daytime airglow emissions. Ann. Geophys., 34, 1019-1030, doi:10.5194/angeo-34-1019-2016

Karan, D. K., and D. Pallamraju, (2017). Small-scale longitudinal variations in the daytime equatorial thermospheric wave dynamics as inferred from oxygen dayglow emissions. J. Geophys. Res. Space Physics, 122, 6528-6542, doi:10.1002/2017JA023891

Karan, D. K., Daniell, R. E., England, S. L., Martinis, C. R., Eastes, R. W., Burns, A. G., & McClintock, W. E. (2020). First zonal drift velocity measurement of equatorial plasma bubbles (EPBs) from a geostationary orbit using GOLD data. *J. Geophys. Res. Space Physics*, 125, e2020JA028173. https://doi.org/10.1029/2020JA028173

Khadka, S. M., Valladares, C. E., Sheehan, R., & Gerrard, A. J. (2018). Effects of electric field and neutral wind on the asymmetry of equatorial ionization anomaly. Radio Science, 53, 683– 697. https://doi.org/10.1029/2017RS006428

Kil, H., E. R. Talaat, S.-J. Oh, L. J. Paxton, S. L. England, and S.-J. Su (2008). Wave structures of the plasma density and vertical E × B drift in low-latitude F region, *J. Geophys. Res. Space Physics*, 113, A09312, doi:10.1029/2008JA013106

Laundal, K. M., and Richmond, A. D. (2017) Magnetic Coordinate Systems, *Space Sci Rev*, 206, 27-59. https://doi.org/10.1007/s11214-016-0275-y

Lieberman, R. S., Fritts, D. C., Pedatella, N., Doornbos, E., & Ortland, D. A. (2015). Global observations of thermospheric lunar tidal winds. *Journal of Atmospheric and Solar-Terrestrial Physics*, *136*, 126–133. https://doi.org/10.1016/j.jastp.2015.05.019

Liu, H. L., E. R. Talaat, R. G. Roble, R. S. Lieberman, D. M. Riggin, and J. H. Yee (2004), The 6.5-day wave and its seasonal variability in the middle and upper atmosphere, *J Geophys Res-Atmospheres*, *109*(D21), doi:10.1029/2004jd004795

Liu, H., Yamamoto, M. & Lühr,, H. (2009). Wave-4 pattern of the equatorial mass density anomaly: A thermospheric signature of tropical deep convection, *Geophysical Research Letters*, *36*, L18104, doi:10.1029/2009GL039865

Luan, X., and S. C. Solomon (2008), Meridional winds derived from COSMIC radio occultation measurements, J. Geophys. Res., 113, A08302, doi:10.1029/2008JA013089.

Lühr, H., & Manoj, C. (2013). The complete spectrum of the equatorial electrojet related to solar tides: CHAMP observations. *Annales Geophysicae*, *31*, 1315–1331. https://doi.org/10.5194/angeo-31-1315-2013

McClintock, W. E., Eastes, R. W., Beland, S., Bryant, K. B., Burns, A. G., Correira, J., et al. (2020a). Global-scale observations of the limb and disk mission implementation: 2. Observations, data pipeline, and level 1 data products. *J. Geophys. Res. Space Physics*, 125, e2020JA027809. https://doi.org/ 10.1029/2020JA027809

McClintock, W. E., Eastes, R. W., Hoskins, A. C., Siegmund, O. H. W., McPhate, J. B., Krywonos, A., et al. (2020b). Global-scale observations of the limb and disk Mission implementation: 1. Instrument design and early flight performance. *J. Geophys. Res. Space Physics*, 125, e2020JA027797. https://doi.org/ 10.1029/2020JA027797

Paulino, A. R., Batista, P. P., & Batista, I. S. (2013). A global view of the atmospheric lunar semidiurnal tide. *Journal of Geophysical Research: Atmospheres*, *118*, 13128–13139. https://doi.org/10.1002/2013JD019818

Pedatella, N. M., Hagan, M. E., & Maute, A. (2012). The comparative importance of DE3, SE2, and SPW4 on the generation of wavenumber-4 longitude structures in the low-latitude ionosphere during September equinox. *Geophysical Research Letters*, *39*, L19108. https://doi.org/10.1029/2012GL053643

Richmond, A. D. (1995). Ionospheric electrodynamics using magnetic apex coordinates, *J. Geomagn. Geoelectr.*, 47, 191–212, https://doi.org/10.5636/jgg.47.191.

Rodríguez-Zuluaga, J., Stolle, C., Yamazaki, Y., Xiong, C., England, S.L. (2020). A mesoscale wave-like structure in the nighttime equatorial ionization anomaly. *Earth and Space Science*, DOI:10.1002/essoar.10504705.1

Soares, G., Yamazaki, Y., Matzka, J., Pinheiro, K., Morschhauser, A., Stolle, C., & Alken, P. (2018). Equatorial counter electrojet longitudinal and seasonal variability in the American sector. *J. Geophys. Res. Space Physics*, 123, 9906–9920. https://doi.org/ 10.1029/2018JA025968

Thébault, E., Finlay, C.C., Beggan, C.D., Alken, P., Aubert, J., Barroi, O. *et al.* (2015). International Geomagnetic Reference Field: the 12th generation. *Earth Planet Sp* **67,** 79, https://doi.org/10.1186/s40623-015-0228-9

Wang, H., Zheng, Z., Zhang, K., & Wang, W. (2020). Influence of nonmigrating tides and geomagnetic field geometry on the diurnal and longitudinal variations of the equatorial electrojet. *J. Geophys. Res. Space Physics*, 125, e2019JA027631. https://doi.org/ 10.1029/2019JA027631

Yamazaki, Y., Matthias, V., Miyoshi, Y., Stolle, C., Siddiqui, T., Kervalishvili, G., et al. (2020), September 2019 Antarctic sudden stratospheric warming: Quasi-6-day wave burst and ionospheric effects. *Geophys. Res. Lett.*, *47*, e2019GL086577. https://doi.org/10.1029/2019GL086577

Yamazaki, Y., Stolle, C., Matzka, J., Siddiqui, T. A., Lühr, H., & Alken, P. (2017). Longitudinal variation of the lunar tide in the equatorial electrojet. *J. Geophys. Res. Space Physics*, *122*, 12,445–12,463. https://doi.org/10.1002/2017JA024601

Zhang, J. T. & Forbes, J. M. (2013). Lunar tidal winds between 80 and 110 km from UARS/HRDI wind measurements. *J. Geophys. Res. Space Physics*, *118*, 5296–5304. https://doi.org/10.1002/jgra.50420